Sustainable Energy & Fuels

Directly Embedded Ni3S2/Co9S8@S-Doped Carbon Nanofiber Networks as Free-standing Anode for Lithium-ion Batteries

Journal:	*Sustainable Energy & Fuels*
Manuscript ID	SE-ART-02-2020-000320.R1
Article Type:	Paper
Date Submitted by the Author:	25-Sep-2020

Complete List of Authors:	He, Zizhou; University of Louisiana at Lafayette, Chemical Engineering Guo, Hui; University of Louisiana at Lafayette, Chemical Engineering LaCoste, Jed; University of Louisiana at Lafayette, Chemical Engineering Cook, Ryan; University of Louisiana at Lafayette, Chemical Engineering Hussey, Blake; University of Louisiana at Lafayette, Industrial Engineering Zhang, Xu; University of Louisiana at Lafayette, Civil Engineering Gang, Daniel; University of Louisiana at Lafayette, Civil Engineering Hao, Ji; National Renewable Energy Laboratory, Mechanical & Industrial Eng Chen, Liang; Biogen Inc, Technical Development; Biogen Cooke, Peter; New Mexico State University, Electron Microscope Laboratory Yan, Hui; University of Louisiana at Lafayette, Chemistry Fei, Ling; University of Louisiana at Lafayette, Chemical Engineering

ARTICLE

Directly Embedded Ni_3S_2/Co_9S_8@S-Doped Carbon Nanofiber Networks as Free-standing Anode for Lithium-ion Batteries

Received 00th January 20xx,
Accepted 00th January 20xx

DOI: 10.1039/x0xx00000x

Zizhou He,[a] Hui Guo,[a g] Jed D LaCoste,[a] Ryan A Cook,[a] Blake Hussey,[a] Xu Zhang,[c] Daniel Dianchen Gang,[c] Ji Hao,[d] Liang Chen,[e] Peter Cooke,[f] Hui Yan,[b] Ling Fei *[a]

Transition metal sulfides as electrode materials for lithium-ion batteries have attracted significant research attention due to their high theoretical capacity, excellent redox reversibility, and earth abundance. However, this material family still suffers poor conductivity and experiences huge volume changes. Here, we demonstrate a facile and scalable electrospinning method to prepare Ni_3S_2 and Co_9S_8 nanoparticles embedded in sulfur doped carbon nanofiber networks as free-standing anode materials for lithium ion batteries. Similar to literature findings, the coupling of two different metal sulfides indeed synergistically promoted the electrochemical performance. Embedding them within individual carbon nanofibers, not only enhances the intrinsic conductivity, but also provides a highly stable structure, which results in excellent battery performance. Furthermore, the individual carbon nanofibers intertwine with each other to form a free-standing 3D nanofiber network which acts as freeway network for fast electron transfer and the pores between fibers allow easy penetration of electrolyte, namely easy lithium ion access to active nanoparticles. When directly applied as anode in lithium ion batteries, the free-standing nanofiber mat bypassed all slurry making steps and showed excellent cycling stability with a high specific capacity of 528 mAh g^{-1} after 200 cycles at a current density of 300 mA g^{-1}. Good rate capability was also obtained. Additionally, the charge storage process analysis indicated that the pseudocapacitive behavior of the material is attributed to the good performance. This work introduces a facile strategy to simultaneously and *in situ* generate Co_9S_8 and Ni_3S_2 nanoparticles within S-doped carbon fiber matrix via facile electrospinning followed by a one-step heating procedure. It is demonstrated that the free-standing transition bimetallic sulfide nanofibers prepared is very promising for light and small battery application.

Introduction

High-performance Lithium-ion batteries (LIBs) have fascinated the tremendous interest of researchers globally due to the fast growing market of portable electronic devices and electric vehicles.[1-3] However, conventional graphite with a theoretical capacity of 372mAh g^{-1} hinders the developing progress of LIBs.[3] Therefore, developing high capacity, long lifespan, lightweight, and low-cost anode materials is urgent to meet the demand. Many efforts have been done in recent years on earth-abundant and low-cost anode materials to develop next-generation lithium ion batteries.[4] Wherein, transition metal sulfides have shown desirable properties such as high theoretical capacity, conversion mechanism, and high redox reversibility. [5] Among them, nickel and cobalt sulfides are the two most studied materials. For instance, CoS_2, NiS_2, Ni_3S_2, Co_9S_8 have all been intensively studied as anode electrode for Li/Na ion batteries.[6-10]

However, cobalt sulfide and nickel sulfide anode materials are still facing several challenges. Firstly, the poor electrical conductivity and sluggish ion transport kinetics of the materials result in insufficient capacity, low Coulombic efficiency, and poor cycle life.[11,12] Secondly, the conversion-reaction type materials are suffering from huge volume change during the repeated lithiation and de-lithiation process. The pulverization of anode materials will lead to the continuous formation of solid electrolyte interphase (SEI) layer, resulting in low Columbic efficiency and consumption of electrolyte.[13] Lastly, most of the

[a] Department of Chemical Engineering, University of Louisiana at Lafayette, Lafayette, LA 70504, United States E-mail: ling.fei@louisiana.edu
[b] Department of Chemistry, University of Louisiana at Lafayette, Lafayette, LA 70504, United States
[c] Department of Civil Engineering, University of Louisiana at Lafayette, Lafayette, LA, 70504, United States
[d] National Renewable Energy Laboratory, Materials Science Center, Golden, CO 80401, United States
[e] New Jersey Institute to Technology, Newark, NJ 07102, United States
[f] Core University Research Resources Laboratory, New Mexico State University, Las Cruces, NM 88003, United States
[g] School of Chemical Engineering, Zhengzhou University, Zhengzhou 450001, P.R. China

† Footnotes relating to the title and/or authors should appear here.
Electronic Supplementary Information (ESI) available: [details of any supplementary information available should be included here]. See DOI: 10.1039/x0xx00000x

prepared active metal sulfide materials are in powder form which requires a tedious and time-consuming slurry making approach to make electrodes.[14] The slurry-based electrodes also tend to form undesired interfaces, uncontrollable microstructure, limited surface area, as well as increasing cost and weight of the anode materials due to extra binder, conductive materials and current collector required.[14,15] Motivated by the above regards, to enhance the conductivity and performance, metal-based materials are usually combined with carbon materials or embedded in carbon matrices.[16, 17] Carbon matrices can effectively enhance the conductivity, prevent the agglomeration of ultra-fine nanoparticles, as well as releasing the stress of volume change induced by repeated charge and discharge processes.[18, 19] It has also been found that rationally combining and regulating cobalt sulfides with nickel sulfides is a very promising for optimized performance in both energy storage and energy conversion applications. [20-23] For instance, Du et al., prepared defects–enriching foam–like Co_9S_8/Ni_3S_2 nanowire via in-situ vulcanization method and achieved low overpotential of 227 mV and −128 mV for OER and HER, demonstrated an excellent bifunctional electrocatalyst.[24] Wang and co-works reported *in situ* sulfurization strategy to synthesize Ni_3S_2 and Co_9S_8 nanoparticles encapsulated on nitrogen-doped porous carbon as supercapacitor electrode with a superior specific capacitance of 1970.5 F g^{-1} at 0.5 A g^{-1}, high rate capability and a high energy density of 77.1 W h kg^{-1} at 263.3 W kg^{-1}.[25] Zhu's group derived Ni_3S_2/Co_9S_8/N-doped carbon composite form Ni-Co-MOF precursor, the composite materials delivered a superior reversible capacity of 419.87 mAh g^{-1} at 0.1 A g^{-1} and 98.6% capacity retention after 100 charge/discharge cycles as well as outstanding rate capability as an anode materials for sodium ion batteries.[26] Moreover, due to the tedious traditional electrode preparation and weight of non-electrochemically active materials, it is highly desirable to develop free-standing anode materials to bypass the slurry coating procedure and significantly reduce the weight of batteries with no binder, extra conductive materials, and current collectors involved.[14]

Herein, we use a straight-forward, scalable, and low-cost electrospinning technique to embed Co_9S_8-Ni_3S_2 nanoparticles in S-doped Carbon nanofibers networks as free-standing anode materials for LIBs. At nanoscale the nanosized Co_9S_8/ Ni_3S_2 nanoparticles and S-doped carbon nanofibers provide following advantages: (i) the nanosized martials shorten the pathway of Li ion diffusion which further promote the ionic transfer rate and reaction kinetics; (ii) the coupling of Co_9S_8 and Ni_3S_2 nanoparticles can offer synergistic effects; (iii) the structure of nanoparticles rooted in the 1D carbon nanofiber provides excellent mechanical stability. Meanwhile, at microscale these nanofibers networks provide (i) a stable 3D structure with high flexibility; (ii) numerous pores among the networks allow the electrolyte easy penetration and quick access; (iii) porous structure has enough space to alleviate the volume change. Benefitting from above advantages our delicately designed Co_9S_8/Ni_3S_2@S-CNFs exhibited excellent cyclic performance and remarkable rate capability. Specifically, the Co_9S_8/Ni_3S_2@S-CNFs maintained 528 mAh g^{-1} with 99.87% columbic efficiency after 200 charge/discharge cycles at current densities of 300 mA g^{-1}, and high rate capability 395.5 mAh g^{-1} at 1 A g^{-1}. The facile, scalable and cost efficient synthesize approach provides a promising way for developing novel anode materials for LIBs.

Experimental Section

Synthesis of Ni_3S_2/Co_9S_8@S-doped carbon nanofiber networks.

N, N-Dimethylformamide (DMF, ACS grade, VWR), Cobalt (II) acetate tetrahydrate (Co $(CH_3COO)_2 \cdot 4H_2O$, ACS Regent 98%, Sigma Aldrich), Nickel (II) acetate tetrahydrate ($Ni(OCOCH_3)_2 \cdot 4H_2O$, 98%, Sigma Aldrich), sulfur (S, ⩾99.5%, Powder -100 mesh, sublimated, Alfa Aesar), Polyacrylonitrile (PAN, average Mw 150,000, Sigma Aldrich) were used directly without further purification

In a typical procedure, 0.5g of PAN was dissolved into 5g DMF and heated at 80°C overnight to form a homogenously transparent solution. Then 2.3mmol of metal acetates Ni $(OCOCH_3)_2 \cdot 4H_2O$ and $(CH_3COO)_2Co \cdot 4H_2O$ (the ratio of Ni: Co is 1:1 in molar) were added into the obtained 10wt% PAN with vigorous stirring for 1 hr. Then 0.2g S powder was added into the solution. The mixture was well dispersed through ultra-sonication and vigorous stirring. The obtained solution was transferred into a 5mL plastic syringe with 20 gauge, 2 inches, point style 3 needle (Hamilton, USA). The electrospinning was carried out by Pump 11 Elite Infusion Dual Syringe pump (Harvard apparatus, USA). The feeding rate of the pump was set as 15uL min^{-1}. A piece of aluminum foil was used as nanofiber collector. The distance between the collector and the needle was fixed at 15cm, and the working voltage between needle and collector at 17.5 kV.

The as-prepared Ni-Co-S/(PAN)NFs precursor was peel off from the aluminum collector for thermal treatment. The precursor was heat treated in a tube furnace in Nitrogen atmosphere for 1hr at 700°C with a ramp rate of 5°C min^{-1}. After cooling down to room temperature naturally under a nitrogen flow, the Ni_3S_2/Co_9S_8@S-doped carbon nanofiber networks is obtained, Ni_3S_2@S-doped carbon nanofiber networks and Co_9S_8@S-doped carbon nanofiber networks was also synthesized under the same condition without adding $Co/Ni(Ac)_2$ for comparison.

Characterizations.

X-ray diffraction (Rigaku D/Max2500 with CuKα radiation) was employed with a scanning rate of 3° min^{-1} at a 2-theta range of 10-80°. Micromeritics ASAP 2020 was used to determine the BET surface area and pore size distribution. The X–ray photoelectron spectroscopy (XPS) measurements were performed with Al K Alpha X-ray source. The morphology information was obtained using a Thermo Scientific™ Apreo scanning electron microscope (SEM). Transmission electron microscope (TEM) and high resolution TEM (HRTEM) were examined by Tecnai G2 F20. Thermogravimetric analysis (TGA) was performed with TGA-1000 from room temperature to 800°C with a ramp rate of 10°C min^{-1}.

Half-cell battery preparation and electrochemical measurement.

The obtained free-standing Ni_3S_2/Co_9S_8@S-CNFs were cut into 0.9-1.2mg fiber mats and directly used as electrode for LIB. The electrochemical performance of the electrodes was investigated by using CR2032 coin cells with lithium metal foil as the counter and reference electrode. 1 M $LiPF_6$ in a mixture of ethylene carbonate/dimethyl carbonate/diethyl carbonate (EC/DMC/DEC, 1:1:1 in volume) solution was used as the electrolyte. Celgard 2400 film was used as separator. The coin cells were assembled in an argon-filled glovebox with oxygen and water content level lower than 1 ppm. Cyclic voltammetry was measured using a STAT III electrochemical workstation (Princeton Applied Research, USA) at a scan rate of 0.2 mV min^{-1} in the voltage window of 0.01-3 V versus lithium (vs. Li^+/Li). The galvanostatic charge/discharge measurements were performed using a Landt battery testing system in the voltage window of 0.05-3 V (vs. Li^+/Li). The electrochemical impedance spectroscopy (EIS) measurements were conducted after cycling 200 times at room temperature at a range of 100,000 Hz to 0.1Hz.

Results and discussion

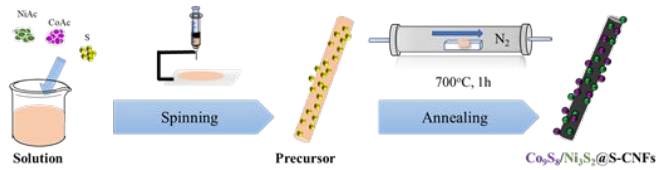

Figure 1. Schematic illustration of the Ni_3S_2/Co_9S_8@S-CNFs synthetic procedures.

The synthetic procedure of Ni_3S_2/Co_9S_8@S-doped Carbon nanofiber CNFs is summarized in Figure 1, nickel and cobalt acetate with desired ratio are dissolved in PAN-DMF solution, then sulfur particles are dispersed in the solution. The fresh $Ni/Co(AC)_2$ nanofiber mats were prepared via electrospinning. The as-spun mats were then subjected to a thermal treatment in N_2. During this process, metal acetates and sulfur react with each other to form metal sulfides, while the PAN polymer backbones simultaneously convert to carbon nanofibers. To understand the phase structures and crystallinity of the obtained samples, XRD was first investigated. As shown in Figure 2a, the strong and sharp diffraction peaks at 2 theta values of, 21.8, 31.1, 37.8, 49.7 and 55.2° correspond to the planes of (1 0 1), (1 1 0), (0 0 3), (1 1 3) and (1 2 2) of the hexagonal Ni_3S_2 phase respectively (JCPDS No. 44-1418). The Bragg peaks located at 29.9, 47.4 and 52.0° could be ascribed to (3 1 1), (5 1 1) and (4 4 0) planes of Co_9S_8 phase (JCPDS No. 19-0364). All the peaks in XRD patterns can be indexed to to the two metal sulfides, which indicates the coexistence of both Co_9S_8 and Ni_3S_2 in the sample. For the single precursor samples, Ni_3S_2 and Co_9S_8 were synthesized correspondingly.

To further understand the surface elements' chemical states and chemical compositions of the Ni_3S_2/Co_9S_8@S-CNFs sample, X-ray photoelectron spectroscopy (XPS) was conducted. The full survey XPS spectrum of Ni_3S_2/Co_9S_8@S-CNFs sample is shown at Figure 2b, the peaks at 856.1 and 797.2 eV correspond to Ni 2p and Co 2p, respectively, while peaks at 284.8 and 162.4 eV are attributed to the C 1s and S 2p, confirming the presence of Ni, Co, S and C elements. The high-resolution spectrum of Ni 2p is shown at Figure 2b, the two satellite peaks at 861.8 and 879.8 eV are shakeup type peaks of Ni.[27] The two peaks located at 874.1 and 855.2 eV correspond to the Ni 2p3/2 and Ni 2p1/2 spin-orbit peaks [28]. The peak at 852.7 eV is the characteristic peak of Ni_3S_2.[29] The Co 2p is shown in Figure 2c, two shakeup satellite peaks at 786.3 and 802.8 eV can be attributed to Co^{3+}.[30]

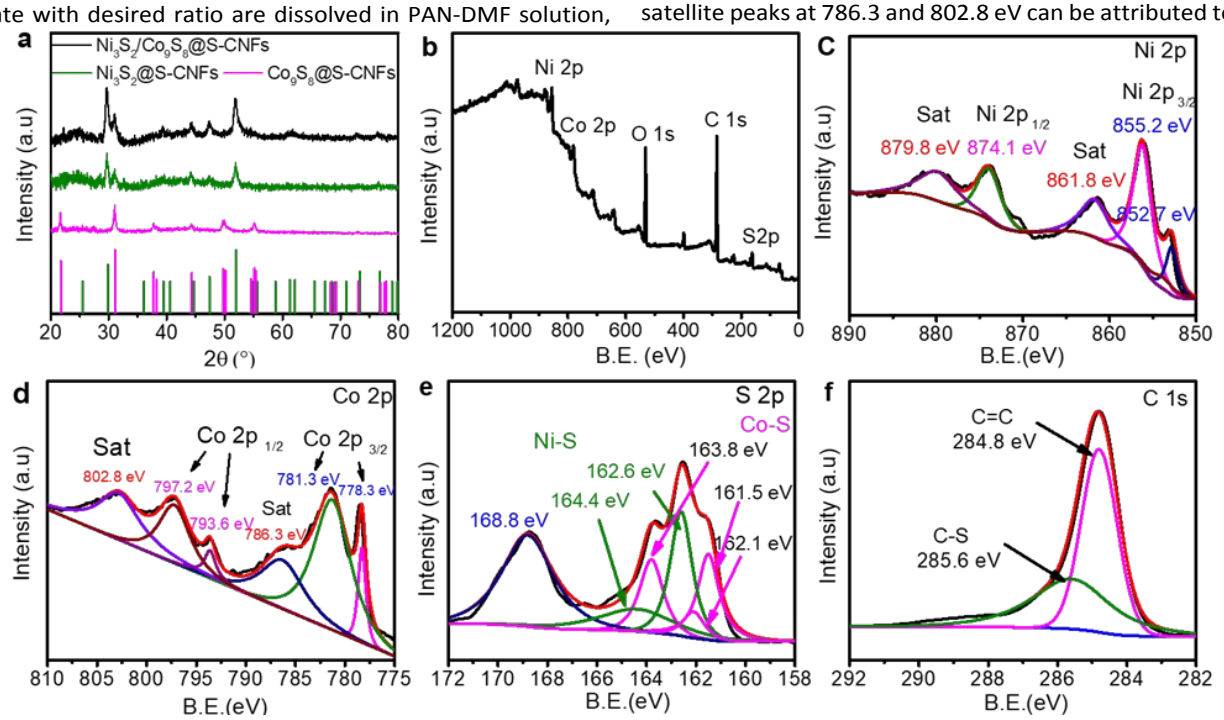

Figure 2(a) XRD pattern of metal sulfides@S-CNFs, (b) XPS survey spectra, (c-f) high-resolution XPS spectra of Ni 2p, Co 2p, S 2p and C 1s of the as-obtained Ni_3S_2/Co_9S_8@S-CNFs composite.

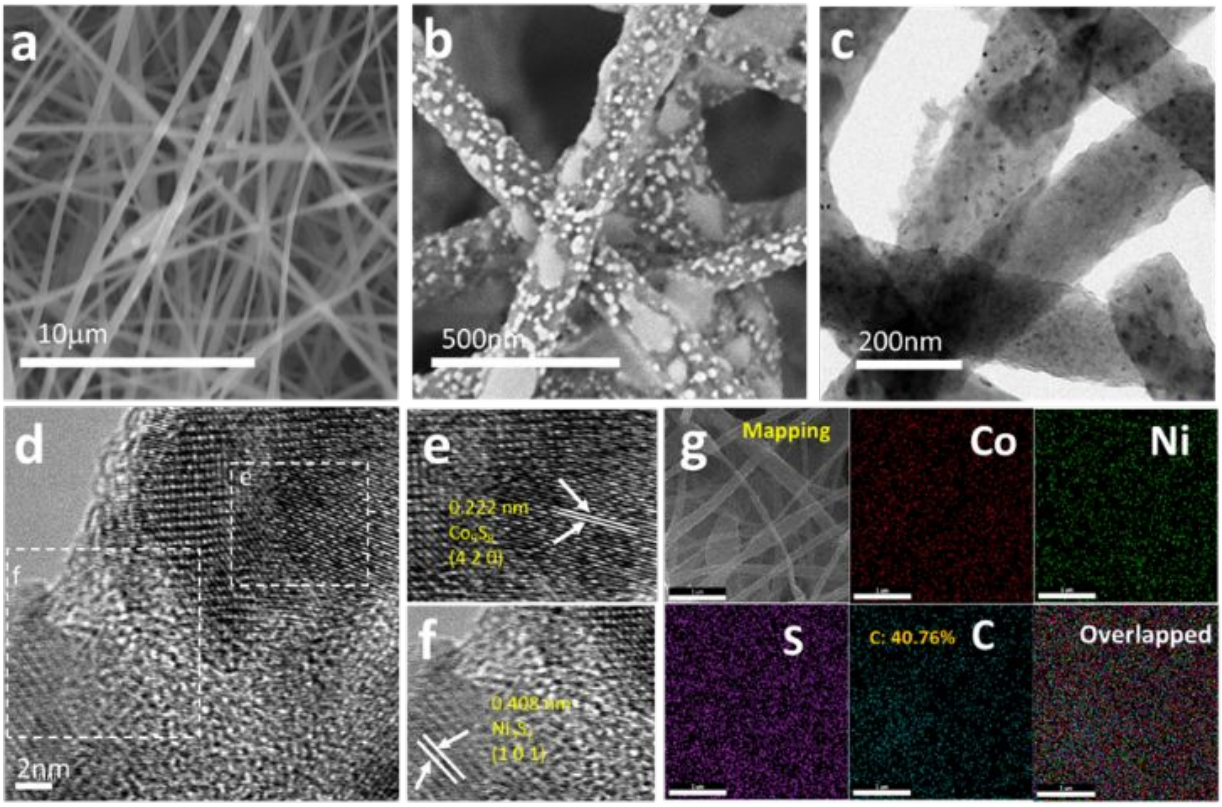

Figure 3 (a) Low-magnification SEM image, (b) high-magnification SEM image, (c) TEM images of the as-prepared the Ni_3S_2/Co_9S_8@S-CNFs composite, (d-f) High-resolution TEM (HRTEM) of the as-prepared Ni_3S_2/Co_9S_8@S-CNFs composite, (g) EDX mapping images of Ni_3S_2/Co_9S_8@S-CNFs composite at scale of 1μm.

Two spin–orbit doublets with peak locations shown at 778.3 and 781.3 eV can be assigned as Co 2p 3/2, while two peaks at 793.6 and 797.2 eV can be described as Co 2p 1/2, respectively. The wide peaks of Co 2p 3/2 and Co 2p 1/2 indicated the co-existence of Co^{2+}/Co^{3+} species and the formation of Co_9S_8.[31] Figure 2d shows the S 2p spectrum, the spectrum can be denoted into six peaks. The presence of 163.8 is ascribed to S 2p 1/2, 161.5 and 162.1 eV corresponded to S 2p 3/2 of Co-S.[22,32,33] Meanwhile, the other two peaks at 164.4 and 162.6 eV corresponded to S 2p 1/2 and S 2p 3/2 of Ni-S. [22] S 2p peak at around 168.8 eV can be indexed to the surface oxidation. The C 1s spectrum is shown in Figure 2f, the peak at 285.6 eV can be ascribed to the C-S bond, indicated the excess sulfur was doped into the carbon nanofiber networks, the cooperate of metal sulfide with S-doped PAN composite can effectively improve the energy density of the electrode.[34,35] The XPS results are in good agreement with the XRD results above, further affirming the co-existence of Co_9S_8 and Ni_3S_2.

The morphology and microstructure of Ni_3S_2/Co_9S_8@S-CNFs were observed by FESEM and shown in Fig 3 a and b. The images show the carbon nanofibers are closely intertwined with each other and form an interconnecting 3D network. There are also lots of void space among the fiber mats, which could allow the electrolyte to easily access the metal sulfides nanoparticles as well as release the stress of volume change of the electrode. Furthermore, the ultrafine metal sulfide nanoparticles were embedded on the surface of the carbon nanofibers without obvious agglomeration, which indicates the active sites present along with the carbon nanofiber network, different from traditional powdered anode materials due to no binder and extra conductive materials involved. The nanosized carbon fiber and metal sulfide nanoparticles exhibit a short Li^+ ion pathway for fast Li^+ ion transfer.

To further investigate the structure and morphology of Ni_3S_2/Co_9S_8@S-CNFs, TEM and HRTEM analyses were carried out. As shown in Figure 3c, the diameter of the carbon nanofibers is around 150nm. Nanoparticles are distributed on the carbon nanofibers without agglomeration, which can maximize the exposure of the active sites while giving enough space to release the stress of volume change. The HRTEM images are shown in Figure 3d-f. From the figure 3d, the particles are not interconnected with each other and two different areas were selected for further investigation. As shown in Figure 3e, the lattice fringe with a spacing of 0.222 nm corresponds to (4 2 0) lattice plane of Co_9S_8. Meanwhile, the lattice fringe space of 0.408 nm assigned to the (1 0 1) crystal plane of Ni_3S_2 is shown at Figure 3f. These results further support the previous conclusions. EDX element mapping was used to explore the metal sulfides distribution and is shown in Figure 3g. From the EDX mapping, Ni, Co, S and C are homogenously distributed on the selected area., Ni and Co ratio are 1:1.02. Moreover, the composition of the as-prepared samples was determined by TGA. Figure S1 shows the calculated weight percentage of carbon in Ni_3S_2/Co_9S_8@S-CNFs,

Ni_3S_2@S-CNFs, Co_9S_8@S-CNFs is 58.5%, 60.5%, and 49.3% respectively. Nitrogen adsorption and desorption measurement was conducted to investigate sample surface area and pore size distribution. Ni_3S_2/Co_9S_8@S-CNFs, Ni_3S_2@S-CNFs, and Co_9S_8@S-CNFs show a BET specific surface area of 371.9, 306.6 and 283.0 $m^2\ g^{-1}$ (Figure S2a), respectively. The pore size of the samples (Fig. S2b) is around 2-4.3 nm. The large specific surface area and mesoporous structure can accelerate ion transfer and help to buffer the volume change in the discharge-charge process, thereby further enhancing the electrochemical performance.

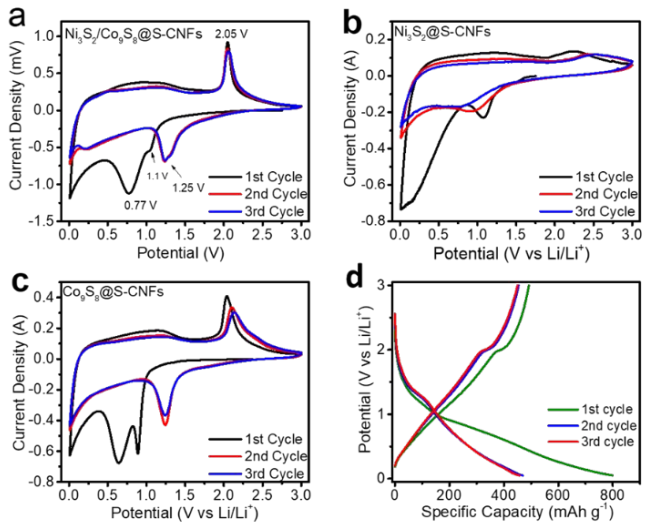

Figure 4 (a-c) CV profiles of the Ni_3S_2/Co_9S_8@S-CNFs, Ni_3S_2@S-CNFs, Co_9S_8@S-CNFs at a scan rate of 0.2 mV s^{-1} in a potential window from 0.01 to 3 V, (d) Galvanostatic charge–discharge profiles of the Ni_3S_2/Co_9S_8@S-CNFs anode at 300 mA g^{-1}.

Cyclic voltammetry (CV) measurements were carried out to evaluate the electrochemical performance of the electrode during lithiation/de-lithiation in a window of 0.01 to 3 V at a scan rate of 0.2mV s^{-1}. Figure 4a shows the CV curves of Ni_3S_2/Co_9S_8@S-CNFs. In the first cycle the cathodic peak at 0.77 V can be ascribed to the formation of a solid electrolyte interface (SEI) layer. The cathodic peak at around 1.1 V is due to the insertion of Li^+ and the formation of Ni and Co ($4Li^+ + 4e^- + Ni_3S_2 \leftrightarrow 3Ni + 2Li_2S$, $16Li^+ + 16e^- + Co_9S_8 \leftrightarrow 9Co + 8Li_2S$).[9,36] The anodic peak located at 2.05 V indicates the formation of metal sulfides.[37-39]. The CV of single metal sulfides Ni_3S_2@CNFs and Co_9S_8@CNFs are compared and shown at Figure 4b and c, the CV curves of two single metal sulfides also reflect a good overlap between the subsequent cycles. The overlapping of the CV curves between cycles reveals the good electrochemical reversibility of the metal sulfides electrodes during the redox process. The good redox reversibility can be attribute to the carbon nanofibers serving as a buffer during the lithiation and de-lithiation processes, releasing the stress of volume expansion and the shrinkage of the embedded metal sulfide nanoparticles. The unique architecture guarantees the excellent cycling performance. Moreover, he Ni_3S_2/Co_9S_8@S-CNFs peaks overlap the best in comparison with that of the single metal electrode: Ni_3S_2@S-CNFs and Co_9S_8@S-CNFs. These results suggest the synergistic effects between these two metal sulfides species.

Figure 4d shows the galvanostatic discharge/charge profiles of Ni_3S_2/Co_9S_8@CNFs at a current density of 300mA g^{-1}. The profile shows a high initial discharge capacity of 799 mAh g^{-1} with a discharge plateau at ~1.1 V result from the formation of Ni and Co, After the first cycle, the plateau shifts to slightly higher voltage, in good agreement with the cathodic peak (~ 1.2V) position shifting trend in the CV scan. The first charge capacity is 492 mAh g^{-1} with a charge plateau at ~2 V due to the de-lithiation. It gives an initial Coulombic efficiency (CE) of 61.6%. The low initial Coulombic efficiency for is caused by the irreversible consumption of lithium ions as well as the formation of solid electrolyte interphase (SEI) layers. Sequentially, the CE of second cycle and third cycle jumped to 96.8% and 98.7%. The second and third cycles shows negligible capacity loss, indicating the good reversibility of the composite anode materials. The above results are also in good agreement with the CV results.

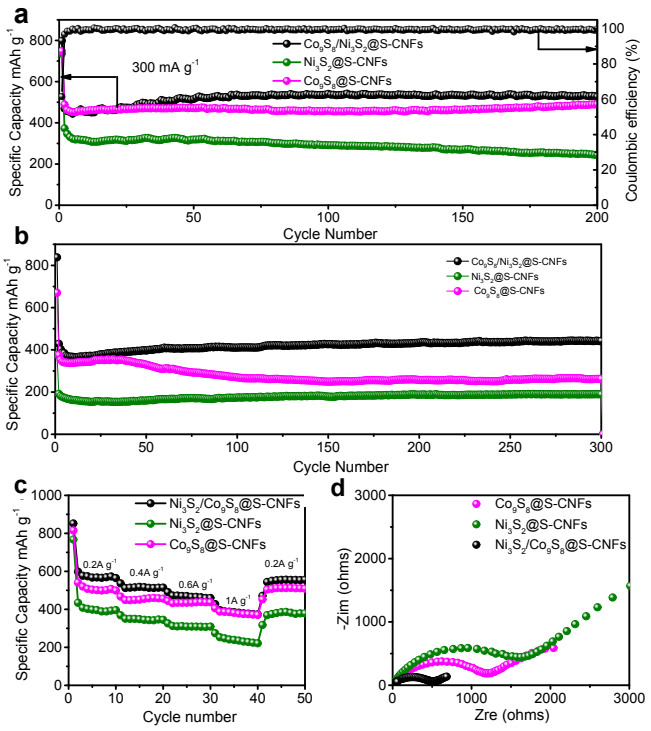

Figure 5 (a) Cycling performance and Coulombic efficiency of the Ni_3S_2/Co_9S_8@S-CNFs, Ni_3S_2@S-CNFs and Co_9S_8@S-CNFs at (a) 300 mA g^{-1} for 200 cycles, (b) 1 A g-1 for 300 cycles. (c) Rate performance of the Ni_3S_2/Co_9S_8@S-CNFs, Ni_3S_2@S-CNFs and Co_9S_8@S-CNFs anodes at different current densities, (d) Electrochemical impedance spectra (EIS) of Ni_3S_2/Co_9S_8@S-CNFs, Ni_3S_2@S-CNFs and Co_9S_8@S-CNFs tested at open circuit potential.

Cyclic performance is one of the most important parameters for electrode materials. The as-synthesized metal sulfides in fiber mats were cut into small pieces and directly applied as free-standing anodes in coin cells for performance evaluation. The samples were tested in the voltage window of 0.05 to 3V vs. Li^+/Li at a current density of 300mA g^{-1} for 200 cycles It is worth mentioning that the current density and specific capacity are based on the mass of the whole electrode. As shown in figure 5a The Ni_3S_2/Co_9S_8@S-CNFs exhibited the highest initial capacity as well as the best cyclic performance compared with the individual metal sulfides, this is due to the synergistic effect between the two metal sulfides. An irreversible capacity loss is

observed after the first cycle, for the Ni_3S_2/Co_9S_8@S-CNFs which can be generally described as the formation of the SEI film and electrolyte decomposition. This phenomenon agrees well with the CV result that the cathodic peaks are present in the first cycle while absent at sequential cycles. After the first cycle there is a slight capacity increment of the electrode which can be ascribed to the gradual activation of the electrode materials, this phenomenon is also observed for transition metal anode materials in previous studies.[5, 40-42] Meanwhile, its Coulombic efficiency increases to more than 99% after the fourth cycle and stayed at this number for the remaining cycles. After 200 cycles, the Ni_3S_2/Co_9S_8@S-CNFs can still maintain 527.8 mAh g^{-1}, nearly 100% columbic efficiency and zero capacity loss demonstrating good long-term cyclic stability. Co_9S_8@S-CNF and Ni_3S_2@S-CNF achieved an initial capacity of 748.5 and 735.6 mAh g^{-1}, after 200 cycles they remain at a specific capacity of 490.3 and 244.6 mAh g^{-1}. the capacity retention is 100% and 66% of the second discharge capacity. The composite electrode exhibited higher initial capacity, specific capacity, and better cyclic retention than Ni_3S_2@S-CNFs and Co_9S_8@S-CNFs, this phenomenon can be ascribed to the synergistic effect of Ni and Co sulfides.[26, 43] To further investigate the synergistic effect, we studied the three composites at a higher cycling current density of 1 A g^{-1}. The results are shown in Fig. 5b. It can be seen that at no obvious difference was observed at the initial 50 cycles for Ni_3S_2/Co_9S_8@S-CNFs and Co_9S_8@S-CNFs, similar to what we observed in the cycle performance at the current of 300 mA g^{-1}. However, after the initial 50 cycles at high current, Ni_3S_2/Co_9S_8@S-CNFs still maintains the highest specific capacity among the three electrodes, and no obvious capacity fading observed in the 300 cycles. While Co_9S_8@S-CNFs shows a decay in the range of 50 to 150 cycles, showing a capacity of 262.3 mA h g^{-1} at the 300th cycle lower than the specific capacity (442.5 mA h g^{-1}) of Ni_3S_2/Co_9S_8@S-CNFs, confirming the good stability and synergistic effect of the bimetallic composites. To investigate the structural stability of the Ni_3S_2/Co_9S_8@S-CNFs anode, SEM image of the anode cycled after 200 cycles at 1 A g^{-1} was obtained. As can be seen in Figure S3, the Ni_3S_2/Co_9S_8@SCNFs electrode still maintained the fiber morphology with a continuously interconnecting 3D network, indicating the remarkable structural stability of the materials. The cyclic stability of this type of electrode is owed to the well-designed structure of the electrode. The robust carbon nanofiber networks can effectively buffer the stress of volume change during the repeated charge and discharge processes, preventing the electrode pulverization.

Rate capability, another important parameter, indicates the electrode capability of fast Li-ion transfer and storage. As shown in Figure 5c,the Ni_3S_2 and Co_9S_8 composite electrode delivers a 10th cycle capacity of 564.6 mAh g^{-1} at 0.2 A g^{-1}, 514.3 mAh g^{-1} at 0.4 A g^{-1}, 459.9 mAh g^{-1} at 0.6 A g^{-1}, and 373.4 mAh g^{-1} at 1 A g^{-1}. When the current density went back to 0.2 A g^{-1}, the capacity is almost fully recovered and maintained a specific capacity of 555.6 mAh g^{-1} (only 9 mAh g^{-1} loss over 50 cycles), showing good rate capacity retention. Other single sulfide electrodes show this similar tendency except a slightly lower specific capacity, which indicates this type of free-standing electrodes have high structure stability and fast ion/electron transfer. The individual fibers connected 3D network structure provides a lot of micrometer pores among the fiber mats which enables the fast penetration of electrolyte, namely, easy access of lithium ions to active materials sites. In addition, the interconnected 1D carbon nanofiber backbones act as freeways for electron transfer as well as buffering the volume change during lithiation and de-lithiation.

To further study the effects of concurrent growth of the two metal species, electrochemical impedance spectroscopy (EIS) was conducted. As Figure 5d shows, all the electrodes exhibit a single semicircle in the high frequency region, and a slope line in the low frequency region. The semicircle at high frequency region is considered to be related with the charge transfer resistance, the slope line at low frequency region is correspond to the lithium ion diffusion in the solid phase [44-46] The Ni_3S_2/Co_9S_8@S-CNFs present the smallest semicircles compare with the Ni_3S_2@S-CNFs and Co_9S_8@S-CNFs electrode, indicating the composite electrode had a smaller charge resistance as well as better charge transfer kinetics than single metal sulfide electrodes, this further affirms the synergistic effects of two metal sulfides. [5,37] The tail in the low-frequency region corresponding to the Li diffusion process, the lithium ions diffusion coefficient were compared according to the equation (S1) by comparing the σ, which is the slope of the line $Z' - \omega^{-1/2}$ (Figure S4). The lithium ions diffusion coefficient is inversely proportional to σ.[47] As shown in Fig. S4, the Ni_3S_2/Co_9S_8@S-CNFs has the least σ and indicates a lager lithium ions diffusion coefficient, which is consistent with the cycling performance results. It is also worth noting that the diffusion coefficient is an important parameter but not necessarily the most decisive one on performance. Yin et. al found that porous structure, N/S doped carbon, good structure stability, and excellent electronic conductivity are more critical than the Li diffusion coefficient for superior rate and long cycling performance. [47] In our case, the specific surface area of Ni_3S_2/Co_9S_8@S-CNFs is highest than the other two. The more porous structure together with the large lithium diffusion coefficient are likely the key to its excellent performance. Moreover, it has also been concluded by Fang et. al that compared to monometal sulfides, two bimetallic sulfides can enhance the ion diffusion and conductivity due to the following two reason: 1) phase boundaries tend to limit the growth of crystal and create crystal defects and active sites for fast ion diffusion, and 2) different redox potentials and out-of-step reactions of the two metal sulfides could alleviate the stress during cycling which is helpful for ion diffusion. [48] Therefore, the bimetallic sulfides outperform the two monometal sulfides.

Significant pseudocapacitive behavior of transition metal chalcogenides has been demonstrated according to previous studies.[5,49,50] Herein, to understand the lithium storage mechanism , the CV measurement of the Ni_3S_2/Co_9S_8@S-CNFs electrode at various scan rates from 0.2 to 1 mV s^{-1} were recorded to study its electrochemical kinetics.[51] As shown in Figure 6a, the peak current density increases with the increase of scan rate and the CV curve shapes remain the same. The lithium storage mechanism can be evaluated by the relationship

of between peak current (i) and scan rate (v) from CV results, based on Eq (1)[52]

$$i=av^b \quad (1)$$

Where a and b are the adjustable parameters. For the analysis, the b-value in the above equation is a factor to determine the type of charge storage mechanism in the electrode: for a diffusion process, the value of b should be 0.5, while for the pseudo-capacitive process, the value of b should be 1.[53] Therefore, to get a certain b value, the Eq (1) can be converted as follow:

$$\log(i) = b\log(v) + \log(a) \quad (2)$$

where the b value can be calculated from the slope of log(i) to log(v) during the respective anodic and cathodic process. Figure 6b shows the b values of the peaks are 0.676, 0.823, 0.825, and 0.907, respectively, revealing the electrochemical reactions involve partial participation of pseudocapacitive behaviors during the redox process. The overall contribution of the pseudo-capacitor at different scan rates were further studied via Eq (3), where the qualitive ratio of pseudo-capacitance to capacity can be calculated by the following equation:[54]

$$i(v) = k_1v + k_2v^{1/2} \quad (3)$$

where i(v) is the total current at a fixed potential which can be divided into two parts: the k_1v is considered as pseudo-capacitance and $k_2v^{1/2}$ is ascribed to the ion diffusion process. The amount of charge storage from diffusion and pseudo-capacitance at 0.2 mV s^{-1} is displayed in Figure 6c. As a result, around 69% of the total capacity is derived from the pseudocapacitive behavior at scan rate of 0.2 mV s^{-1}. Such high percentage of pseudo-capacitive behavior, even at a low scan rate of 0.2 mV s^{-1}, strongly indicates that the electrochemical process of the Ni_3S_2/Co_9S_8@S-CNFs electrode is dominated by the pseudocapacitive behavior. This large contribution of the surface-induced capacitive effect can be ascribed to the highly exposed active sites along the 1D nanofibers, which provides plenty of active sites for Li ions to be stored on the surface of the electrode.[55]

As Figure 6d shows, the contribution of the pseudo-capacitance is increased with an increment of scan rate, while the diffusion contribution is decreased. At the scan rate of 0.2, 0.4, 0.6, 0.8, and 1 mv s^{-1} the contribution of the pseudo-capacitance is about 69%, 73%, 77%, 80%, and 83%, respectively. This behavior indicates the pseudo-capacitance is dominant at high scan rates. This is because of the well-designed structure providing a lot of active sites and short Li^+ ion diffusion pathways, all contributing to high capacity and high-rate performance.[5] It's also worth to mention the decrease of the diffusion contribution is due to the limit diffusion kinetic and increased ohmic resistance with increasing scan rate. [56]

Conclusions

In summary, we have successfully embedded Ni_3S_2 and Co_9S_8 nanoparticles on the S-doped carbon nanofiber networks as anode electrode for high performance LIBs. The composite materials show improved electrochemical performance with excellent cyclic performance and rate capability. The excellent performance should be ascribed to the well-designed structure that is able to alleviate the volume change stress, enhance the conductivity, promote the reaction kinetics. Our result shows the electrode delivers a high ratability with a high 799 mAh g^{-1} initial discharge capacity after 200 cycles it stabilized at 528 mAh g^{-1} with 99.87% columbic efficiency at a current density of 300 mA g^{-1}. Furthermore, good rate capability of 373.4 mAh g^{-1} at 1 A $g^{-1}$is achieved We believe our work provides a possible way for developing novel transition metal sulfide anode materials for small and light LIBs.

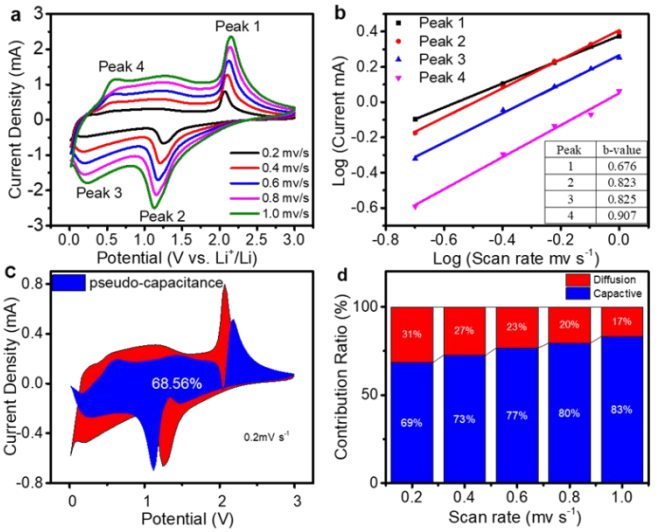

Figure 6 (a) CV curves of the cell at different scan rates after ten cycles, (b) The fitted lines and ln (peak current) vs ln (scan rate) plots at different oxidation and reduction state, (c) The pseudo-capacitance contribution (0.2 mV s^{-1}) is 69% and shown by the blue region, (d) The pseudo-capacitance contribution at different scan rates.

Conflicts of interest

There are no conflicts to declare

Acknowledgements

We acknowledge the financial support from NASA EPSCoR/Louisiana Board of Regents (Sponsor ID: LEQSF-EPS (2020)-RAP-31). Dr. Fei acknowledges Chevron Corporation for providing her Chevron Endowed Professorship in Chemical Engineering at UL Lafayette. Ryan A Cook acknowledges the fund support from UL Lafayette College of Engineering Research Apprentice program and the University Undergraduate Research Mini-Grant program.

Notes and references

1. S. Goriparti, E. Miele, F. De Angelis, E. Di Fabrizio, R. Proietti Zaccaria and C. Capiglia, *J. Power Sources* 2014**, *257***, 421-443.
2. J. B. Goodenough and K. S. Park, *J. Am. Chem. Soc.* 2013, **135**, 1167-1176.

3. M. Armand and J. M. Tarascon, *Nature*, 2008, **451**, 652-657.
4. P. Poizot, S. Laruelle, S. Grugeon, L. Dupont and J. M. Tarascon, *Nature*, 2000, **407**, 496-499.
5. T. Yang, Y. Liu, D. Yang, B. Deng, Z. Huang, C. D. Ling, H. Liu, G. Wang, Z. Guo and R. Zheng, *Energy Storage Mater.,* 2019, **17**, 374-384.
6. J. Zhang, L. Yu and X. W. D. Lou, *Nano Res.*, 2017, **10**, 4298-4304.
7. J. Li, J. Li, Z. Ding, X. Zhang, Y. Li, T. Lu, Y. Yao, W. Mai and L. Pan, *Chem. Eng. J.*, 2019, **378**.
8. S. Ni, X. Yang and T. Li, *Mater. Chem. Phys.*, 2012, **132**, 1103-1107.
9. Y. Zhou, D. Yan, H. Xu, S. Liu, J. Yang and Y. Qian, *Nanoscale*, 2015, **7**, 3520-3525.
10. J. Li, J. Li, D. Yan, S. Hou, X. Xu, T. Lu, Y. Yao, W. Mai and L. Pan, *J. Mater. Chem. A*, 2018, **6**, 6595-6605.
11. Q. Zhou, L. Liu, Z. Huang, L. Yi, X. Wang and G. Cao, *J. Mater. Chem. A*, 2016, **4**, 5505-5516.
12. X. Y. Yu, H. Hu, Y. Wang, H. Chen and X. W. Lou, *Angew. Chem. Int. Ed. Engl.*, 2015, **54**, 7395-7398.
13. Y. Tan, M. Liang, P. Lou, Z. Cui, X. Guo, W. Sun and X. Yu, *ACS Appl. Mater. Interfaces*, 2016, **8**, 14488-14493.
14. L. Fei, B. P. Williams, S. H. Yoo, J. M. Carlin and Y. L. Joo, *Chem. Commun.*, 2016, **52**, 1501-1504.
15. T. Y. Ma, S. Dai and S. Z. Qiao, *Mater. Today*, 2016, **19**, 265-273.
16. X. Zhang, R. Zhao, Q. Wu, W. Li, C. Shen, L. Ni, H. Yan, G. Diao and M. Chen, *ACS Nano*, 2017, **11**, 8429-8436.
17. W. Li, R. Zhao, K. Zhou, C. Shen, X. Zhang, H. Wu, L. Ni, H. Yan, G. Diao and M. Chen, *J. Mater. Chem. A*, 2019, **7**, 8443-8450.
18. J. Xia, L. Liu, S. Jamil, J. Xie, H. Yan, Y. Yuan, Y. Zhang, S. Nie, J. Pan, X. Wang and G. Cao, *Energy Storage Mater.*, 2019, **17**, 1-11.
19. N. Zhang, S. Gan, T. Wu, W. Ma, D. Han and L. Niu, *ACS Appl. Mater. Interfaces*, 2015, **7**, 12193-12202.
20. J. Xie, X. Li, H. Lai, Z. Zhao, J. Li, W. Zhang, W. Xie, Y. Liu and W. Mai, *Angew. Chem. Int. Ed. Engl.*, 2019, **58**, 14740-14747.
21. D. Ghosh and C. K. Das, *ACS Appl. Mater. Interfaces*, 2015, **7**, 1122-1131.
22. Y. Yang, H. Yao, Z. Yu, S. M. Islam, H. He, M. Yuan, Y. Yue, K. Xu, W. Hao, G. Sun, H. Li, S. Ma, P. Zapol and M. G. Kanatzidis, *J. Am. Chem. Soc.*, 2019, **141**, 10417-10430.
23. S. Zhuo, Y. Shi, L. Liu, R. Li, L. Shi, D. H. Anjum, Y. Han and P. Wang, *Nat. Commun.*, 2018, **9**, 3132.
24. F. Du, L. Shi, Y. Zhang, T. Li, J. Wang, G. Wen, A. Alsaedi, T. Hayat, Y. Zhou and Z. Zou, *Appl. Catal. B Environ.*, 2019, **253**, 246-252.
25. S. Wang, Z. Xiao, S. Zhai, H. Wang, W. Cai, L. Qin, J. Huang, D. Zhao, Z. Li and Q. An, *J. Mater. Chem. A*, 2019, **7**, 17345-17356.
26. X. Liu, F. Zou, K. Liu, Z. Qiang, C. J. Taubert, P. Ustriyana, B. D. Vogt and Y. Zhu, *J. Mater. Chem. A*, 2017, **5**, 11781-11787.
27. N. Cheng, Q. Liu, A. M. Asiri, W. Xing and X. Sun, *J. Mater. Chem. A*, 2015, **3**, 23207-23212.
28. X. Zhong, L. Zhang, J. Tang, J. Chai, J. Xu, L. Cao, M. Yang, M. Yang, W. Kong, S. Wang, H. Cheng, Z. Lu, C. Cheng, B. Xu and H. Pan, *J. Mater. Chem. A*, 2017, **5**, 17954-17962.
29. W. Zhou, X.-J. Wu, X. Cao, X. Huang, C. Tan, J. Tian, H. Liu, J. Wang and H. Zhang, *Energy Environ. Sci.*, 2013, **6**.
30. S. Zhang, D. Li, S. Chen, X. Yang, X. Zhao, Q. Zhao, S. Komarneni and D. Yang, *J. Mater. Chem. A*, 2017, **5**, 12453-12461.
31. X. Cao, X. *Electrochim. Acta*, Zheng, J. Tian, C. Jin, K. Ke and R. Yang, 2016, **191**, 776-783.
32. H. Zhu, J. Zhang, R. Yanzhang, M. Du, Q. Wang, G. Gao, J. Wu, G. Wu, M. Zhang, B. Liu, J. Yao and X. Zhang, *Adv. Mater.*, 2015, **27**, 4752-4759.
33. S. Dou, L. Tao, J. Huo, S. Wang and L. Dai, *Energy Environ. Sci.*, 2016, **9**, 1320-1326.
34. Z. Wang, Y. Dong, H. Li, Z. Zhao, H. B. Wu, C. Hao, S. Liu, J. Qiu and X. W. Lou, *Nat. Commun.*, 2014, **5**, 5002.
35. A. K. Haridas, J. Heo, Y. Liu, H. J. Ahn, X. Zhao, Z. Deng, M. Agostini, A. Matic, K. K. Cho and J. H. Ahn, *ACS Appl. Mater. Interfaces*, 2019, **11**, 29924-29933.
36. P. Yu, L. Wang, J. Wang, D. Zhao, C. Tian, L. Zhao and H. Yu, *RSC Adv.*, 2016, **6**, 48083-48088.
37. W. Zhou, J.-L. Zheng, Y.-H. Yue and L. Guo, *Nano Energy*, 2015, **11**, 428-435.
38. C.-H. Lai, K.-W. Huang, J.-H. Cheng, C.-Y. Lee, W.-F. Lee, C.-T. Huang, B.-J. Hwang and L.-J. Chen, *J. Mater. Chem.*, 2009, **19**.
39. J. Zhou, X. Liu, J. Zhou, H. Zhao, N. Lin, L. Zhu, Y. Zhu, G. Wang and Y. Qian, *Nanoscale Horiz.*, 2019, **4**, 182-189.
40. D. Cai, B. Liu, D. Wang, L. Wang, Y. Liu, B. Qu, X. Duan, Q. Li and T. Wang, *J. Mater. Chem. A*, 2016, **4**, 183-192.
41. W. Cao, W. Wang, H. Shi, J. Wang, M. Cao, Y. Liang and M. Zhu, *Nano Res.*, 2018, **11**, 1437-1446.
42. H. Yu, H. Fan, B. Yadian, H. Tan, W. Liu, H. H. Hng, Y. Huang and Q. Yan, *ACS Appl. Mater. Interfaces*, 2015, **7**, 26751-26757.
43. J. Lv, D. Bai, L. Yang, Y. Guo, H. Yan and S. Xu, *Chem. Commun.*, 2018, **54**, 8909-8912.
44. J. Qiu, P. Zhang, M. Ling, S. Li, P. Liu, H. Zhao and S. Zhang, *ACS Appl. Mater. Interfaces*, 2012, **4**, 3636-3642.
45. Z. Gao, N. Song, Y. Zhang and X. Li, *Nano Lett.*, 2015, **15**, 8194-8203.
46. Y. F. Yuan, L. W. Ye, D. Zhang, F. Chen, M. Zhu, L. N. Wang, S. M. Yin, G. S. Cai and S. Y. Guo, *Electrochim. Acta*, 2019, **299**, 289-297.
47. B. Yin, X. Cao, A. Pan, Z. Luo, S. Dinesh, J. Lin, Y. Tang, S. Liang and G. Cao, *Adv. Sci.*, 2018, **5**, 1800829.
48. G. Fang, Z. Wu, J. Zhou, C. Zhu, X. Cao, T. Lin, Y. Chen, C. Wang, A. Pan and S. Liang, *Adv. Energy Mater.*, 2018, **8**.
49. J. B. Cook, H.-S. Kim, T. C. Lin, C.-H. Lai, B. Dunn and S. H. Tolbert, *Adv. Energy Mater.*, 2017, **7**.
50. W. Yang, N. Luo, C. Zheng, S. Huang and M. Wei, *Small*, 2019, DOI: 10.1002/smll.201903904, e1903904.
51. T. Brezesinski, J. Wang, S. H. Tolbert and B. Dunn, *Nat. Mater.*, 2010, **9**, 146-151.
52. A. G. Dylla, G. Henkelman and K. J. Stevenson, *Acc. Chem. Res.*, 2013, **46**, 1104-1112.
53. I. E. Rauda, V. Augustyn, B. Dunn and S. H. Tolbert, *Acc. Chem. Res.*, 2013, **46**, 1113-1124.
54. J. B. Cook, H.-S. Kim, Y. Yan, J. S. Ko, S. Robbennolt, B. Dunn and S. H. Tolbert, *Adv. Energy Mater.*, 2016, **6**.
55. W. Cha, I. Y. Kim, J. M. Lee, S. Kim, K. Ramadass, K. Gopalakrishnan, S. Premkumar, S. Umapathy and A. Vinu, *ACS Appl. Mater. Interfaces*, 2019, **11**, 27192-27199.

56. A. Jagadale, X. Zhou, D. Blaisdell and S. Yang, *Sci. Rep.*, 2018, **8**, 1602.